Nano-Micro Letters

ISSN 2311-6706
e-ISSN 2150-5551
CN 31-2103/TB

ARTICLE

https://doi.org/10.1007/s40820-020-00511-4

Cite as
Nano-Micro Lett.
(2020) 12:171

Received: 19 May 2020
Accepted: 3 August 2020
Published online: 25 August 2020

Tuning Interface Bridging Between $MoSe_2$ and Three-Dimensional Carbon Framework by Incorporation of MoC Intermediate to Boost Lithium Storage Capability

Jing Chen[1], Yilin Luo[1], Wenchao Zhang[3], Yu Qiao[2], Xinxin Cao[1], Xuefang Xie[1], Haoshen Zhou[2], Anqiang Pan[1,4] ✉, Shuquan Liang[1] ✉

✉ Anqiang Pan, pananqiang@csu.edu.cn; Shuquan Liang, lsq@csu.edu.cn

[1] School of Materials Science and Engineering, Central South University, Changsha 410083, Hunan, People's Republic of China

[2] Energy Interface Technology Group, National Institute of Advanced Industrial Science and Technology, 1-1-1, Umezono, Tsukuba 305-8568, Japan

[3] Institute for Superconducting and Electronic Materials, School of Mechanical, Materials, Mechatronics and Biomedical Engineering, Faculty of Engineering and Information Sciences, University of Wollongong, Wollongong, NSW 2500, Australia

[4] Key Laboratory of Advanced Energy Materials Chemistry (Ministry of Education), Nankai University, Tianjin 300071, People's Republic of China

HIGHLIGHTS

- $MoSe_2$/MoC/C multiphase boundaries boost ionic transfer kinetics.
- $MoSe_2$ (5–10 nm) with rich edge sites is uniformly coated in N-doped framework.
- The obtained $MoSe_2$ nanodots achieved ultralong cycle performance in LIBs and high capacity retention in full cell.

ABSTRACT Interface engineering has been widely explored to improve the electrochemical performances of composite electrodes, which governs the interface charge transfer, electron transportation, and structural stability. Herein, MoC is incorporated into $MoSe_2$/C composite as an intermediate phase to alter the bridging between $MoSe_2$- and nitrogen-doped three-dimensional (3D) carbon framework as $MoSe_2$/MoC/N–C connection, which greatly improve the structural stability, electronic conductivity, and interfacial charge transfer. Moreover, the incorporation of MoC into the composites inhibits the overgrowth of $MoSe_2$ nanosheets on the 3D carbon framework, producing much smaller $MoSe_2$ nanodots. The obtained $MoSe_2$ nanodots with fewer layers, rich edge sites, and heteroatom doping ensure the good kinetics to promote pseudo-capacitance contributions. Employing as anode material for lithium-ion batteries, it shows ultralong cycle life (with 90% capacity retention after 5000 cycles at 2 A g^{-1}) and excellent rate capability. Moreover, the constructed $LiFePO_4$//$MoSe_2$/MoC/N–C full cell exhibits over 86% capacity retention at 2 A g^{-1} after 300 cycles. The results demonstrate the effectiveness of the interface engineering by incorporation of MoC as interface bridging intermediate to boost the lithium storage capability, which can be extended as a potential general strategy for the interface engineering of composite materials.

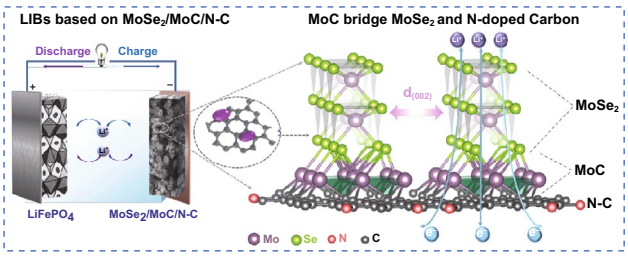

KEYWORDS Interface engineering; Porous carbon framework; $MoSe_2$ nanodots; MoC; Heterostructure; Battery

1 Introduction

Transition metal dichalcogenide (TMD) materials MX_2 (M = transition metal; X = chalcogen) with lamellar structure have received broad attentions in the fields of batteries, supercapacitors, catalysts, and sensors due to their large layer distance and high surface area [1–6]. Among them, transition metal selenides (MSe_2) have higher conductivity than the corresponding sulfides (MS_2) and oxides (MO_2). Moreover, the bond strength of M–Se is weaker than M–S or M–O, which is kinetically favorable for conversion reactions [7, 8]. Specifically, molybdenum diselenide ($MoSe_2$) possesses large interlayer distance (0.65 nm, two times larger than that of commercial graphite) because of weak van der Waals forces and relatively high electronic conductivity (1×10^{-3} S m^{-1}) triggered from the narrow band gap (1.1 eV) [9–11], making it a promising electrode material for lithium-ion batteries (LIBs). However, $MoSe_2$ electrode still suffers from large volume variations, inherently low conductivity, and adverse reaction during cycling, which leads to severe capacity fading and inferior rate performance [8, 12–15].

To address aforementioned concerns, great efforts have been focused on nano-/microstructure design and carbon modification. In general, nanosized materials can effectively eliminate the effect of volume variations, providing a short ion diffusion length and offer large pseudo-capacitance, which lead to fast ionic migration and superior rate performance [16–19]. However, the large contact area between electrode materials and electrolyte may increase the side reaction and cause the dissolution of the electrode materials. Another effective strategy is making TMD and carbon composites, in which carbon serves as a soft matrix to buffer the volume variations and fast electron conductor [20–23]. Particularly, three-dimensional (3D) porous carbon skeletons are preferred because of their extra capability to tolerant the volume changes. Zhao et al. have achieved high-performance Co_3O_4 lithium-ion battery anode by employing 3D carbon network substrate [24]. Cao and co-workers synthesized 3D porous Mo_2C/C architecture to improve the lithium storage capacity [25]. Although the electrochemical performances are improved greatly, the long-term cycling stability is rear reported. The difficult can be attributed to the weak bonding between the active material and carbon substrates, or the mismatch of their volume variations, which degrade the structural stability of the electrode upon long-term cycling.

Interface engineering can introduce distortions, dislocations, and lattice defects, with distinguished electronic structures, which are long-range disorder and, hence, can lower the activation barrier, thus boosting reaction kinetics [5, 26, 27]. More recently, through interface coupling by chemical bonds, previous theoretical calculation and practical experiments both have revealed that Mo–O–C or Mo–C bonds between carbon and $MoSe_2$ can effectively enhance electronic conductivity and structure stability through the interface [28, 29]. However, the portion of the chemical bonding between the active material and substrate is still too limited to stabilize structure. Therefore, it is highly expected to increase the chemical bonds at the interface or develop new strategy to improve the stability of composites, in particular for long-term cycling applications. Introducing intermediate material to bridge the active material and the substrate presents to be a wise choice. Comparing to $MoSe_2$, MoC owns intrinsic higher electrical conductivity and chemical stability [30–32]. The structural stability and charge transportation will be greatly improved by the incorporation of MoC into the composite, which bridges $MoSe_2$ and carbon substrates by $MoSe_2$–MoC–carbon connection.

Herein, we reported the temperature-induced one-step incorporation of MoC as an intermediate phase to bridge $MoSe_2$- and N-doped three-dimensional carbon framework, which essentially improve the interfacial structural stability of the composite. Moreover, the in situ formed MoC can effectively inhibit the overgrowth of $MoSe_2$ nanocrystals and constrain $MoSe_2$ to nanodots with few layers and rich edge sites. The obtained materials guarantee bi-continuous fast electron/ion transport and highly reversible conversion reactions and enable fast reaction kinetics and good structural stability. As expected, 3D porous $MoSe_2$/MoC/N–C electrodes deliver much improved long-term cycling stability. It retains 90% of its initial capacity after 5000 cycles at 2 A g^{-1}. And the assembled $LiFePO_4$//$MoSe_2$/MoC/N–C full cell also exhibits a high reversible capacity and good cyclic stability (86% capacity retention after 300 cycles at 2 A g^{-1}).

2 Experimental

2.1 Synthesis of 3D Porous $MoSe_2$/MoC@N–C and $MoSe_2$/C

All chemicals were used as received without further purification. 0.4 g of $(NH_4)_6Mo_7O_{24}{\cdot}4H_2O$, 0.4 g of PVP and 1.2 g

https://doi.org/10.1007/s40820-020-00511-4

of NaCl were dissolved in 30 mL of distilled water. After stirring for 1 h at room temperature, the resulting transparent solution was quick-frozen with liquid nitrogen and further freeze-dried for 30 h at − 40 °C in vacuum to yield a precursor. Then, the precursor was mixed with selenium powders in a mass ratio of 5:1 and annealed under Ar atmosphere at 600 or 800 °C for 3 h with a heating rate of 5 °C min^{-1}. After that, 3D porous $MoSe_2$/C and $MoSe_2$/MoC@N–C were obtained after dissolving NaCl in deionized water. For comparison, bare $MoSe_2$ was prepared by annealing a mixture of ammonium molybdate tetrahydrate and selenium powders at 800 °C for 3 h with a heating rate of 5 °C min^{-1} under Ar atmosphere. MoC/C could be obtained by annealing the same precursor under Ar atmosphere at 750 °C for 3 h with a heating rate of 5 °C min^{-1} without Se powder.

2.2 Characterizations

The structure features of the samples were performed by X-ray diffraction (XRD, Rigaku D/max 2500), Raman microscope (Horiba Jobin–Yvon, Lab Ram Aramis), and X-ray photoelectron spectroscopy (XPS, AXIS-ULTRA DLD-600 W system). The morphologies and energy-dispersive X-ray (EDX) element mapping (SEM, Quanta FEG 250) were characterized by scanning electron microscopy and Transmission electron microscope (TEM, JEOL JEM-2100F). Specific surface areas were calculated by the multipoint Brunauer–Emmett–Teller (BET) method.

2.3 Electrode Fabrication and Electrochemical Measurement

Electrochemical performances were evaluated by using 2032-type coin half cells with metallic lithium served as the anode. Working electrodes were prepared by casting a slurry containing the active material (70 wt%), Super P (15 wt%) and sodium carboxymethyl cellulose (15 wt%) dispersed in distilled water on a clean Cu foil current collector. Each electrode in our experiment has an area of 1.1304 cm^{-2}, and the loading of active material for each electrode was about 1.0–1.2 mg. All cells were assembled in a glove box (Mbraun, Germany) filled with ultrahigh-purity argon. For LIB assembly, polypropylene membrane and 1 M $LiPF_6$ in ethylene carbonate (EC)–dimethyl carbonate (DMC)–diethyl carbonate (DEC) (1:1:1 in volume) were used as a separator and electrolyte, respectively. As for the assembly of full cell, a pre-lithiation procedure was carried on to compensate the loss of lithium during the initial cycle in half cell. To ensure the maximized material utilization and reasonably evaluate the electrochemical property of the $MoSe_2$/MoC@N–C, the full cell in this work was assembled based on the capacity ratio of ≈ 1.2:1 between the $LiFePO_4$ cathode and $MoSe_2$/MoC/N–C anode.

The cyclic voltammetry (CV) measurements were taken on an electrochemical workstation (CHI660C) at a scan rate of 0.1 mV S^{-1} in the voltage range of 0.01–3 V (vs. Li^+/Li). The electrochemical impedance spectrometry (EIS) data were collected on a ZAHNER-IM6ex electrochemical workstation (ZAHNER Co., Germany) in the frequency range of 100 kHz to 10 mHz. Land battery tester (Land CT 2001A, Wuhan, China) was employed to investigate the galvanostatic charge/discharge performances, and all tests were conducted at room temperature.

3 Results and Discussion

3.1 Formation Mechanism and Structure Characterization of Materials

The synthetic mechanism of the 3D porous $MoSe_2$/MoC/N–C and advantages of the structure are shown in Scheme 1. As a nitrogen-rich carbon network source, polyvinyl pyrrolidone (PVP) is a nonionic surfactant that can adsorb molybdate ions to facilitate the in situ formation of Mo–C bond. When the precursor annealed at high temperature, molybdenum can react with carbon to form MoC. Selenium powder is used to form $MoSe_2$. And NaCl is employed as a template to create pores due to its environmental friendliness, cheapness, and high melting point. The obtained porous structure with 3D electrically conductive pathways possesses both large surface areas and abundant mass transportation channels, guaranteeing the good contact between electrolyte and electrode interface. More importantly, as shown in Scheme 1b, different from previous reports of $MoSe_2$/C composites, $MoSe_2$ and carbon substrate were bridged by highly conductive MoC interphase, forming a tri-phase MoC/N–C heterostructure where the $MoSe_2$/MoC/N–C connection can boost fast charge kinetics and highly reversible conversion, leading to improved long-term cycling stability. This $MoSe_2$/MoC/N–C connection also

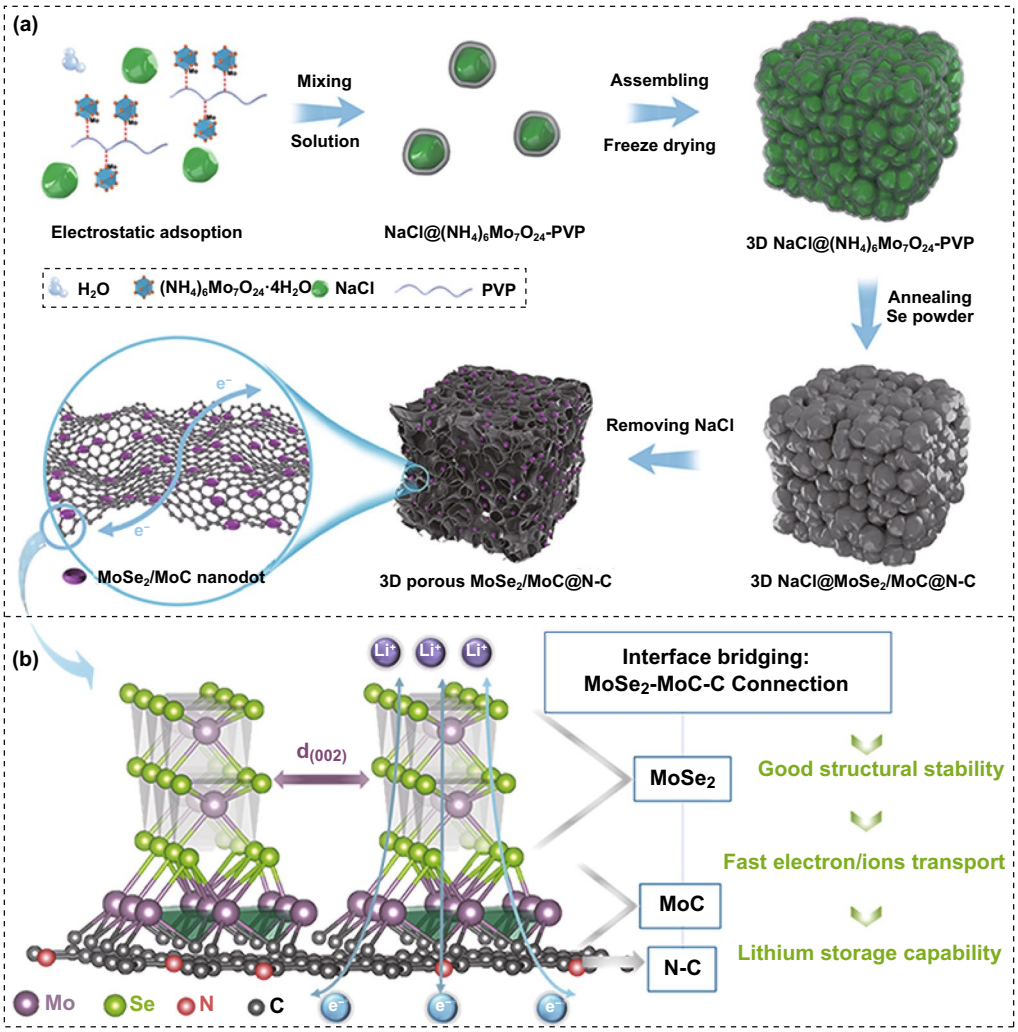

Scheme 1 Schematic illustration of **a** the formation process of interconnected 3D porous structure of obtained $MoSe_2$/MoC/N–C nanocomposite and **b** model of interface bridging between $MoSe_2$- and N-doped carbon network

induced the growth of $MoSe_2$ to terrace-terminated mode (illustrated in Scheme S1), resulting few-layered $MoSe_2$ nanodots, and thus, greatly contributed to pseudo-capacitance effect and guaranteed the fast the ion diffusion kinetics, which synergistically boosts lithium storage capability.

More specific characterizations of material are comprehensively presented within Figs. 1 and 2. As shown in Fig. 1a (XRD patterns), the as-prepared sample annealed under 800 °C exhibited two additional diffraction peaks located at 35.7° and 48.7° compared to $MoSe_2$ phase (JCPDS No. 29-0914, 2H-$MoSe_2$), which are corresponding to MoC phase (JCPDS No. 45-1015). Specifically, compared to bare $MoSe_2$ and $MoSe_2$/C, the broadened diffraction peaks in $MoSe_2$/MoC/N–C sample indicate its relatively small crystal size. And the weaker intensity of (002) peak indicates rich defects along [002] direction [28]. Unlike the crystallinity normally increase with the rising of the annealing temperature (800 °C), the intensity and crystallites of $MoSe_2$ in the composite decreased. The XRD patterns suggest the growth of $MoSe_2$ may be changed. No detection of XRD peaks for Mo metal indicates the easier formation of MoC and its stable state at 800 °C.

As for the Raman characterization, all the samples present two bands at around 240 and 280 cm^{-1} (Fig. 1b), which are assigned to the A_g^1 and E_{2g}^1 stretching of $MoSe_2$, respectively. The A_g^1-related peak is attributed to the

https://doi.org/10.1007/s40820-020-00511-4

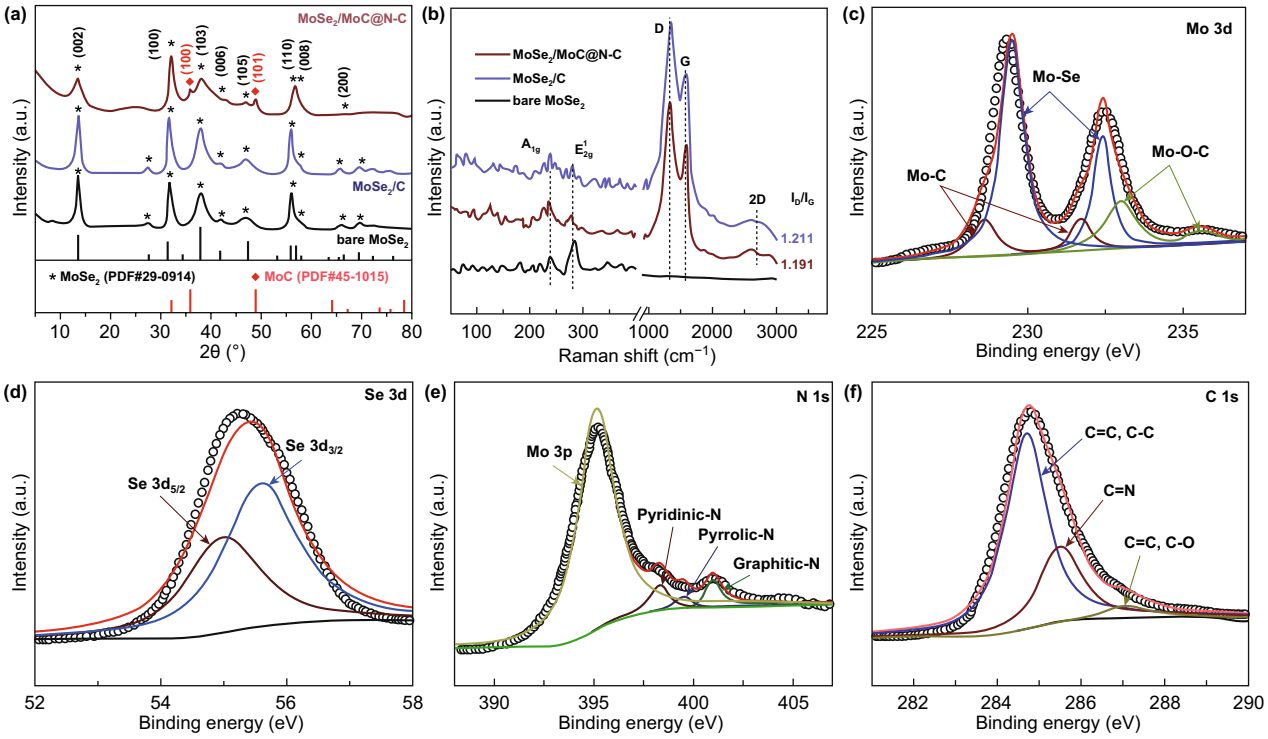

Fig. 1 **a** XRD patterns and **b** Raman spectrum of bare $MoSe_2$, $MoSe_2$/C, and $MoSe_2$/MoC/N–C; XPS spectra of $MoSe_2$/MoC/N–C: **c** Mo 3d, **d** Se 3d, **e** N 1 s, and **f** C 1 s

exclusive peak of $MoSe_2$ 2H structure, preferred for edge-terminated mode, while the E^1_{2g} peak is assigned to the characteristic peaks of $MoSe_2$ 1T structure, favored for terrace-terminated $MoSe_2$ [13, 33, 34]. Thus, 1T/2H phases of $MoSe_2$ were consisted in three synthesized samples. Moreover, the increased intensity ratio of A^1_g/E^1_{2g} from bare $MoSe_2$ to $MoSe_2$/MoC/N–C suggests the decreased thickness and increased exposed edge sites of $MoSe_2$ in the interconnected 3D porous structure. The D and G bands locating at 1375 and 1590 cm^{-1} confirm the presence of disordered and graphitic carbon structures within interconnected 3D porous superstructure, respectively [12, 35, 36]. The content of carbon was calculated as 34.6% in the $MoSe_2$/C composite, determined by thermal gravimetric (TG) analysis as shown in Fig. S1, and the residual product (MoO_3) is verified by the XRD pattern in the inset. Furthermore, the XPS spectrum shows the existence of Mo, Se, C, and N elements (Fig. S2). The Mo 3d XPS spectrum (Fig. 1c) shows three doublets: 229.5 and 232.4 eV assigned to Mo–Se bonds, 233.3 and 235.7 eV corresponding to Mo–O–C, and 228.6 and 231.7 eV corresponding to Mo–C bonding [13, 24, 33, 37], confirming the formation of MoC in the $MoSe_2$/MoC/N–C nanocomposite, which is consistent with the XRD results. More importantly, the formation of Mo–O–C and Mo–C bonds could be demonstrated, which implies the strong electronic coupling at the interface between MoC, $MoSe_2$and 3D porous carbon. The formation of Mo–O–C bonds was mainly due to the combination of Mo ion with the carbonyl group (–C=O) in the PVP. Previous experiments and theoretical calculations have shown that Mo–C or Mo–O–C bonds in $MoSe_2$/C nanocomposite could facilitate the ion and electron transportation in the composite [28, 29]. For the Se 3d XPS spectra, two typical peaks at 55.5 and 54.8 eV correspond to the $3d_{3/2}$ and $3d_{5/2}$ peaks of Se^{2-} in the $MoSe_2$/MoC/N–C nanocomposite (Fig. 1d). The C 1*s* profile in Fig. 1f can be deconvoluted into three individual peaks at 285.5 eV (C–N), 284.7 eV (C–C and C=C), and 287.1 eV (C–O, C=O). The formation of C–N bonds demonstrated the nitrogen doping in the carbon substrate. Furthermore, the N 1*s* peaks are partially overlapped with Mo 3*p* peaks (at 395.1 eV) and could be deconvoluted as graphitic N at 400.9 eV, pyrrolic-N at 399.5 eV, and pyridinic-N at 398.3 eV [13, 24, 33, 37]. The nitrogen doping could

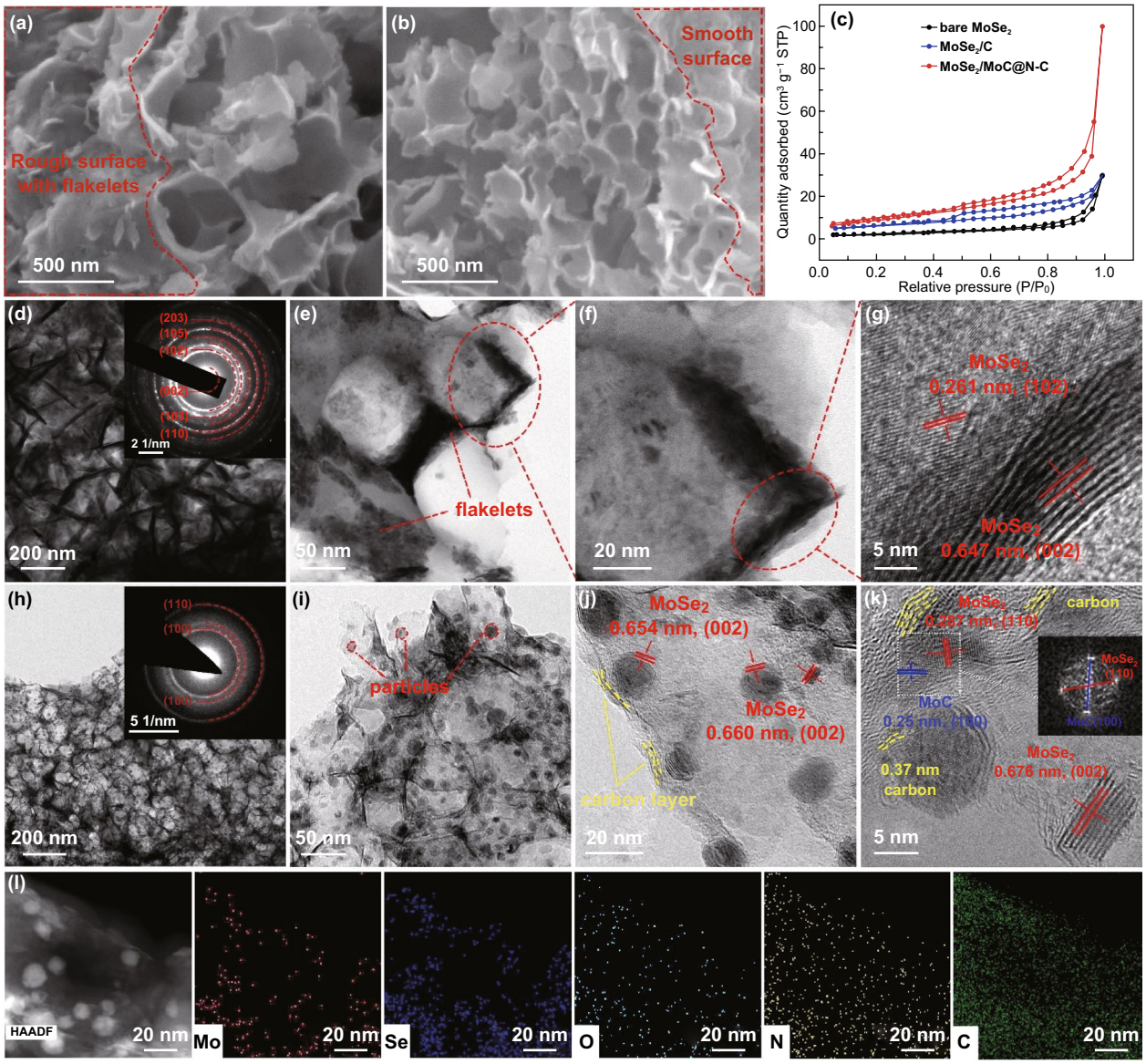

Fig. 2 SEM images of **a** $MoSe_2$/C and **b** $MoSe_2$/MoC/N–C; **c** statistical data of surface area; **d–f** TEM and **g** HRTEM images of $MoSe_2$/C; **h–j** TEM and **k** HRTEM images of $MoSe_2$/MoC/N–C (inset: FFT of the selected area); **l** elemental mappings of $MoSe_2$/MoC/N–C

introduce more defects and electroactive sites, resulting in good electron transportation in the composite [38].

As depicted in Fig. S3, pure $MoSe_2$ agglomerates into irregular bulks about 20 μm in width. However, as expected, both $MoSe_2$/C and $MoSe_2$/MoC/N–C possessed a highly interconnected three-dimensional porous network with microstructure (Fig. 2). Interestingly, compared to $MoSe_2$/C, $MoSe_2$/MoC/N–C possesses more uniform pore distribution and thinner network thickness (Fig. 2a, b), which can be further confirmed by TEM observations. The uniform pores (about 80 nm) were created by dissolution of NaCl and the release of gases generated during the selenization. As a result, $MoSe_2$/MoC/N–C composite possesses a large Brunauer–Emmett–Teller specific surface area (S_{BET}) of 34.9 $m^2\ g^{-1}$ and $MoSe_2$@N–C possesses specific surface area of 21.5 $m^2\ g^{-1}$, both of which are much larger than 7.9 $m^2\ g^{-1}$ of bare $MoSe_2$ (Fig. 2c). The detailed information of pore size distribution of three samples is shown in Fig. S4. The high S_{BET} and the porous structure are favorable to ion diffusion and structural stability upon cycling.

https://doi.org/10.1007/s40820-020-00511-4

The semitransparent TEM images further indicate the ultrathin network structure of composites (Fig. 2d–k). When we zoom in, for $MoSe_2$/C sample, thick nanosheets with various sizes were attached to or embedded in the network (Fig. 2e, f), which were proved as $MoSe_2$ (Fig. 2g). In general, agglomeration is more likely to occur in high-temperature reactions. However, $MoSe_2$ crystals in $MoSe_2$/MoC/N–C sample (800 °C) are smaller and more dispersed than those in $MoSe_2$/N–C (600 °C). In comparison, for $MoSe_2$/MoC/N–C, the interconnected 3D porous architecture (Fig. 2h) is more obvious than that of $MoSe_2$/C. Moreover, a large number of small particles with size of 5–20 nm are uniformly distributed in smooth N–C network (Fig. 2i, j). These small sizes are favorable to the lithium-ion intercalation/deintercalation. Figure 2j further indicates that the thin carbon layer totally coats the small $MoSe_2$/MoC nanocrystal. The N–C capsule can effectively protect nanosized $MoSe_2$ from adverse reactions and facilitate fast electron transport.

The high-resolution TEM (HRTEM) image (Fig. 2g, k) reveals that nanodots in $MoSe_2$/MoC/N–C nanocomposite is composed of only a few layers (about 10 layers), much less than that of $MoSe_2$/C. Furthermore, the layer distance of $MoSe_2$/MoC/N–C (0.676 nm) is also larger than that of $MoSe_2$/C (0.647 nm), which facilitate fast Li-ion transportations. Notably, the interlayer distances of 0.25 nm marked in Fig. 2k is assigned to the distance spacing of (100) plane of MoC crystal, which is in close contact with $MoSe_2$ crystals. And the corresponding fast Fourier transform (FFT) result (inset in Fig. 2k) revealed the (110) and (100) plane of the $MoSe_2$ and MoC, respectively, further confirming the formation of $MoSe_2$/MoC heterostructure. Because the carbon source of MoC is from the carbonized PVP (N–C substrate), the in situ formed MoC is bonded to carbon framework, which can be confirmed by Mo-C and Mo–O-C bonding from XPS (Fig. 1c). Therefore, it can be deduced that the intermediate MoC bridges N–C framework and $MoSe_2$ through $MoSe_2$/MoC/N–C connection, strengthening the interfacial coupling in tri-phase $MoSe_2$/MoC/N–C superstructure, which enable fast charge transportation and good structural stability. And defects in $MoSe_2$/MoC/N–C multiphase boundaries with distinguished electronic structures could lower the activation barrier, thus boosting reaction kinetics. In addition, around nanodots, some graphitic carbon fringes about 0.37 nm are observed, as indicated by the yellow dotted line (Fig. 2k). The graphitic carbon in the composite can provide conductive pathways for rapid electron transfer even at high current densities.

By comparing the structure of $MoSe_2$/C and $MoSe_2$/MoC/N–C composites (Fig. 2), it can be concluded that the in situ formed intermediate MoC could effectively inhibit the overgrowth of $MoSe_2$ nanocrystals and expand their layer spacing. During the heating process, partial Mo reacted with Se to form $MoSe_2$ first. When the reaction temperature rose to 800 °C, Mo and carbon reacted to form dispersion MoC, while $MoSe_2$ crystals continue to nucleate and grow, forming $MoSe_2$/MoC/C heterojunction. This $MoSe_2$/MoC/C connection induced the growth of $MoSe_2$ to terrace-terminated mode (illustrated in Scheme S1), resulting in few-layered and small-sized $MoSe_2$ nanodots. Furthermore, the in situ formed MoC can pin heterostructure, preventing crystals form and agglomerating. The dark-field scanning TEM and the corresponding elemental mapping images of $MoSe_2$/MoC/N–C reveal that Mo, Se, O, N, and C are evenly distributed on the ultrathin carbon wall (Figs. 2l and S12). The distribution of Mo and Se concentrate on the location of nanodots, indicating the formation of $MoSe_2$ again, while the uniform distribution of N throughout the sample demonstrates that the 3D porous framework consists of N-doped carbon.

3.2 Electrochemical Lithium-Ion Storage Performance and Reaction Kinetics

The $MoSe_2$/MoC/N–C composite was assembled to half and full cells to investigate their electrochemical performances. The cyclic voltammetry (CV) curves obtained during the initial 3 cycles (at a scanning rate of 0.1 mV s^{-1}) exhibit multiple redox reactions for $MoSe_2$/MoC/N–C electrode (Fig. 3a). During the first cathodic sweep, four obvious reduction peaks at 0.605, 0.782, 1.175, and 2.138 V can be clearly observed. The small peak at 1.175 V can be assigned to the reduction of MoC, and other peaks are well documented for $MoSe_2$ [14, 31, 39]. These peaks are also consistent with the results in CV curves of $MoSe_2$/C and MoC/C counterparts in Figs. S7b and S8c. The reduction peak at 0.782 V can be ascribed to the insertion of Li ion into $MoSe_2$ to form Li_xMoSe_2, and the subsequent peak at 0.605 V can be ascribed to the reduction of Li_xMoSe_2 to Mo and Li_2Se [28, 44]. In the first cycle, two oxidation peaks at 1.428 and 2.138 V correspond to a partial oxidation of Mo metal to

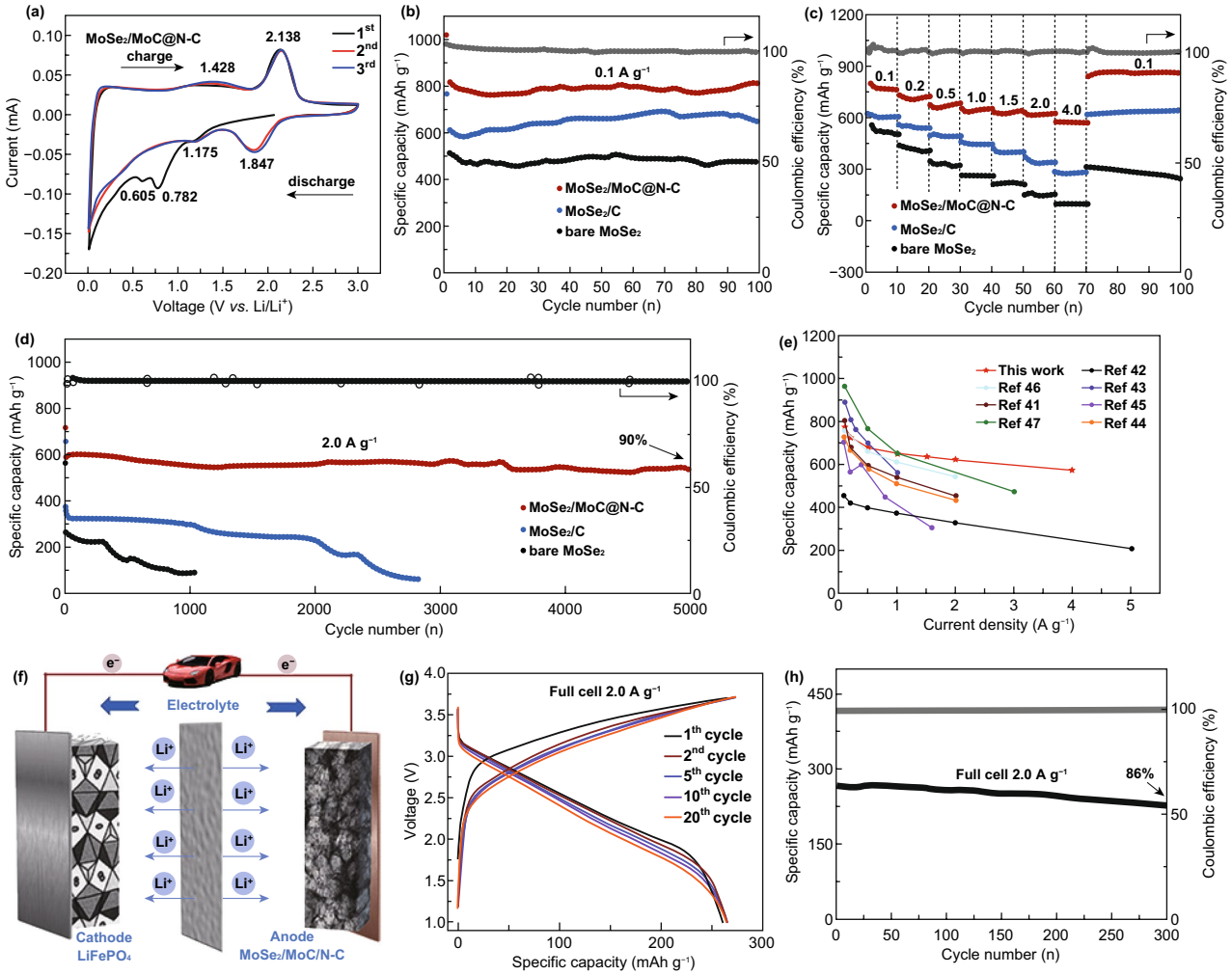

Fig. 3 **a** Initial three cyclic voltammograms cycles of the $MoSe_2$/MoC/N–C electrode at a scan rate of 0.1 mV s^{-1}. **b** Cycling performance (0.1 A g^{-1}), **c** rate performances, and **d** long-term cycling performances (2 A g^{-1}) of bare $MoSe_2$, $MoSe_2$/C, and $MoSe_2$/MoC/N–C electrodes between 0.01 and 3 V versus Li/Li^+. **e** Comparison plot of rate performance between this work and previously published $MoSe_2$/C composite-related works. **f** Schematic illustration of the $LiFePO_4$//$MoSe_2$/MoC/N–C full-cell configuration. **g** Charge/discharge profiles of the full cell. **h** Cycling performance of the full cell at 0.1 A g^{-1}

form $MoSe_2$ and oxidation of Li_2Se to Se, respectively [14]. In the next cycles, reduction peaks at 0.605 and 0.782 V disappeared, but new peak at 1.847 V can be obtained for the conversion of Li_xMoSe_2 to Mo and Li_2Se [41–44], while two oxidation peaks at 2.138 and 1.428 V remain constant. The shift of peaks of $MoSe_2$ involved with the irreversible reaction [43–47]. However, the peak at 1.175 V corresponding to MoC remains constant (the same as this peak at CV curves of MoC/C in Fig. S8c), suggesting the reversible conversion reactions of MoC [31, 39]. Figure S6 presents charge/discharge profiles of selected cycles of $MoSe_2$/MoC/N–C electrode; after initial cycle, two platforms at around 1.8 and 1.2 V can be ascribed to the contribution of $MoSe_2$ and MoC in the composite electrode, respectively. The result is the same as peak voltages in CV curves. The initial charge and discharge capacities are 812 and 1014 mAh g^{-1}, respectively, corresponding to a coulombic efficiency (CE) of 80.1%, which is higher than most reported $MoSe_2$ electrodes [14, 24, 40, 41]. The irreversible capacity in the initial cycle may come from the formation of a SEI film [24]. From the second cycle, all charge/discharge curves were close to overlapping, indicating the excellent electrode reversibility.

Figure 3b compares the cycling performances of three samples at 0.1 A g^{-1}. $MoSe_2$/MoC/N–C nanocomposite exhibits the highest specific capacity of around 800 mAh g^{-1} compared to $MoSe_2$/C (650 mAh g^{-1}) and bare $MoSe_2$

 https://doi.org/10.1007/s40820-020-00511-4

(440 mAh g^{-1}). This result demonstrates that constructing interconnected 3D porous carbon-modified nanocomposite can indeed improve the capability of storage Li ion. By the way, in the early stages of the cycling (Fig. 3b), the capacities of $MoSe_2$/C and $MoSe_2$/MoC/N–C rise slightly, which may be related to the activation of the electrode material. $MoSe_2$/MoC/N–C shows the best rate performance (Fig. 3c). The electrode delivered average capacities of 773, 720, 680, 648, 634, 622, and 575 mAh g^{-1} at 0.1, 0.2, 0.5, 1.0, 1.5 2.0, and 4.0 A g^{-1}, respectively, and it can fully recover and even displays the higher capacity when the current density switched back to 0.1 A g^{-1}. However, $MoSe_2$/C and pure $MoSe_2$ undergo apparent capacity loss at high rates in different degrees. The obtained high specific capacity and good rate capability of the $MoSe_2$/MoC/N–C electrode also show superiority compared to many other carbon-modified $MoSe_2$ anode materials (Fig. 3e) [41–47], which demonstrates the advantage of fast interfacial charge transfer through $MoSe_2$/MoC/N–C connection again.

What makes the $MoSe_2$/MoC/N–C electrode more attractive is its ultralong cycle life with the capacity retention of 90% and a high capacity of 535 mAh g^{-1} after 5000 cycles at 2 A g^{-1} (Fig. 3d). In sharp contrast, for $MoSe_2$/C electrode, a capacity of 308 mAh g^{-1} can be maintained just 1000 cycles, and bare $MoSe_2$ even undergoes a sharply fading after 295 cycles.

To confirm the role of MoC in lithium storage, three-dimensional porous MoC/C was prepared through a similar routine of preparing $MoSe_2$/MoC/N–C. The SEM image (Fig. S8b) shows that MoC/C possesses the similar morphology to $MoSe_2$/MoC/C composites (Fig. 2b). The cyclic voltammetry (CV) curves and the cycling performance of MoC/C composite as anode for LIBs were further carried out to study the lithium storage properties of MoC (Fig. S8c, d). As a result, it exhibits the capacity close to that of $MoSe_2$/MoC/N–C and good electrochemical reversibility. Meanwhile, the weight ratio between $MoSe_2$ and MoC was estimate as 51:2 (molar ratio of 54:5) according to Table S1, indicating that MoC possess relatively low contents in the electrodes. Therefore, the direct capacity contribution from MoC to the whole electrode is relatively limited. However, MoC plays an important role in the interfacial structure regulation, including more stable chemical binding and reduced $MoSe_2$ particle size, which is more correlated with the rate performance and structural stability. $MoSe_2$/MoC/N–C shows a higher capacity than $MoSe_2$/C mainly because its smaller $MoSe_2$ nanodots can provide more lithium storage sites. The MoC connected $MoSe_2$ and N–C network through C/MoC/$MoSe_2$ multiphase boundaries, enabling fast electron/ion transport and structural stability through interface, resulting in good rate performance and structural stability.

Encouraged by the excellent performance $MoSe_2$/MoC/N–C electrode in half cell, we assembled a lithium-ion full by pairing with the commercial $LiFePO_4$ cathode (Fig. 3f). As shown in Fig. 3g, the full cell displays a complete discharge plateau at about 2.3 V with a reversible capacity of about 267 mAh g^{-1} at 2 A g^{-1}. Meanwhile, its energy density was calculated as 93.9 Wh kg^{-1} at the high power density of 698.5 W kg^{-1}. It is still a great challenge to obtain stable cycling performance of the full-cell batteries based on conversion reaction electrodes because of the low coulombic efficiency and large consumption of lithium sources during the initial cycles to form SEI layers. However, the $LiFePO_4$//$MoSe_2$/MoC/N–C full cell exhibits good capacity retention of 86% after 300 cycles (Fig. 3h), indicating the good cyclic stability.

The reaction kinetics of $MoSe_2$/MoC/N–C electrode was systematically studied by CV measurements, galvanostatic intermittent titration technique (GITT) and EIS spectroscopy. The electrochemical kinetics in the as-prepared electrodes could be considered as capacitive-dominated and diffusion-controlled from the CV curves (Figs. 4a and S9). After detailed calculations as detailed descriptions in the Supporting Information, the higher b value of the $MoSe_2$/MoC/N–C electrode (0.90 vs. 0.69 of the $MoSe_2$/C at the cathodic peak) reveals a faster ionic transportation which resulted in a better rate performance (Fig. 4b) [48–51]. Figure 4c shows the calculated voltage profile for the capacitive current (colored region) at the scan rate of 1.2 mV s^{-1}. As a result, 74% of the total capacity is calculated as the capacitive contribution for the $MoSe_2$/MoC/N–C electrode, higher than 64% of the $MoSe_2$/C. Furthermore, Fig. 4d compares the calculated capacitive contribution of two electrodes at various scan rates. The ratios of capacitive contribution of $MoSe_2$/MoC/N–C electrode are always higher than those of $MoSe_2$/C, with a maximum value of 90% at 2 mV s^{-1}. The large pseudo-capacitive contribution would play a critical role to be benefit for ionic transportation in the electrode [48, 49], which boosting high-rate Li-ion storage capability.

The diffusion-controlled reaction kinetics of samples were further analyzed in depth by GITT (Fig. S11). As shown in Fig. 4e, f, the diffusion coefficient of $MoSe_2$/MoC/N–C

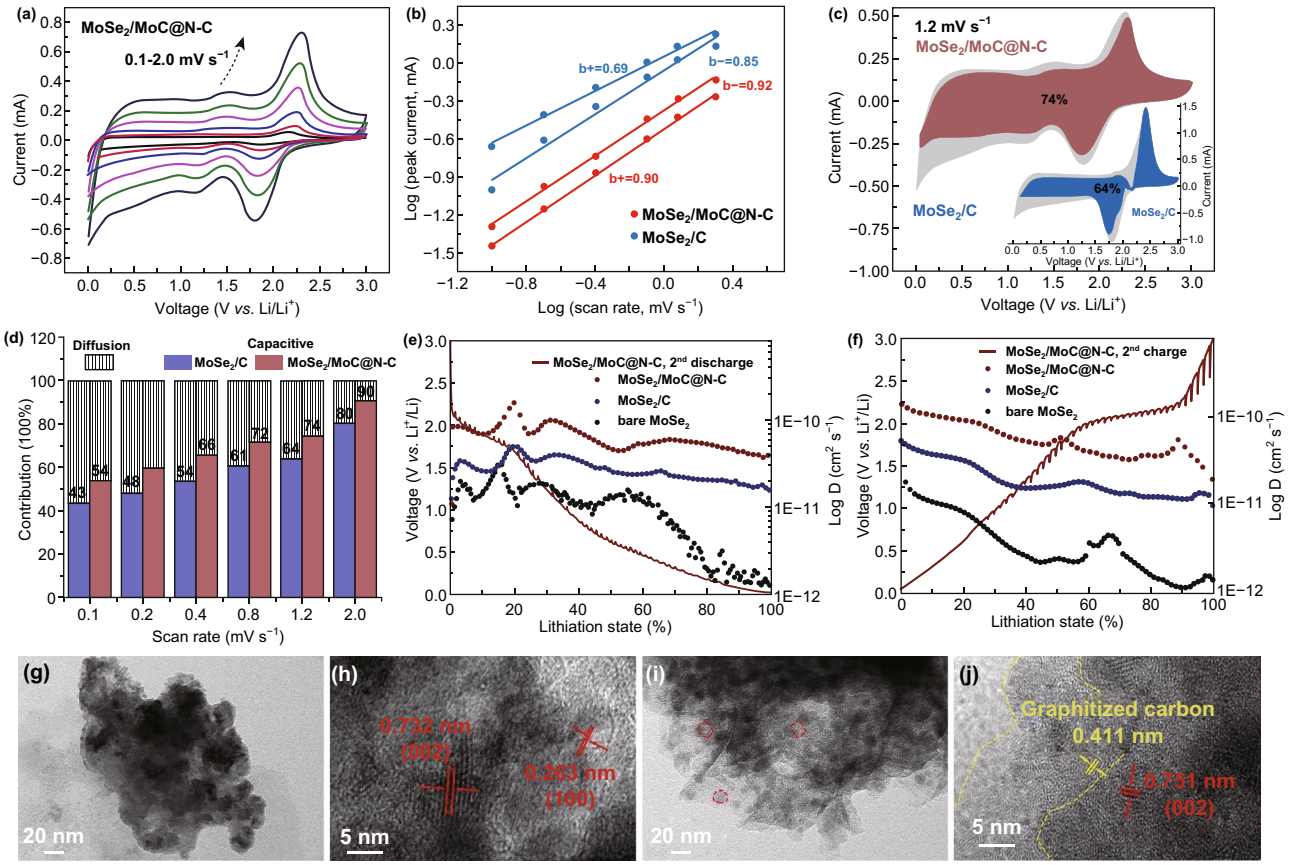

Fig. 4 Quantitative capacitive analysis of lithium storage behavior. **a** CV curves at different scan rates of the $MoSe_2$/MoC/N–C electrode. **b** Relationship between logarithm cathodic peak current and logarithm scan rates. **c** Capacitive contribution (red wine for $MoSe_2$/MoC/N–C and navy blue for $MoSe_2$/C) and diffusion contribution (gray) at 1.2 mV s^{-1}. **d** Normalized contribution ratio of capacitive capacities at different scan rates; GITT curves and the corresponding Li-ion diffusion coefficient at **e** the 2nd discharge process and **f** the 2nd charge process. TEM and corresponding HRTEM images of **g, h** $MoSe_2$/C and **i, j** $MoSe_2$/MoC/N–C electrodes after 100 cycles at 2 A g^{-1} (full charge state)

electrode is about 3.93e−11 to 1.55e−10 cm^2 s^{-1}, higher than those of $MoSe_2$/C and bare $MoSe_2$, suggesting that expanded layer distance, rich edge defect $MoSe_2$ nanocrystal, and $MoSe_2$/MoC/N–C connection definitely facilitate fast Li-ion diffusion kinetics. The electrochemical impedance spectra (EIS) results (Fig. S10 and Table S2) demonstrated that charge transfer resistances (R_{ct}) of $MoSe_2$/MoC/N–C (43 Ω) are smaller than those of $MoSe_2$/C (72 Ω) and bare $MoSe_2$ (557 Ω), suggesting that $MoSe_2$/MoC/N–C shows the fastest interface kinetics. All above analysis suggested that the optimized interconnected 3D porous N–C framework and stronger electronic coupling at interface through $MoSe_2$/MoC/N–C connection facilitate reaction kinetics.

Ex situ TEM images were employed to investigate the structural integrity of $MoSe_2$/MoC/N–C electrode after certain cycles at 2 A g^{-1}. Compared to the ex situ TEM images of as-synthesized $MoSe_2$/C (Fig. S13A1 and A2), the $MoSe_2$ flakes in the $MoSe_2$/C electrode (Fig. 4g or Fig. S13A3) were broken into small pieces and form aggregates after 100 cycles, which may further lead to electrode pulverization and indicate its inferior structure stability. However, at the same cycles, $MoSe_2$/MoC/N–C electrode (Fig. 4i or Fig S13B3) displayed the good preservation of interconnected 3D porous network structure, and the small nanocrystals encapsulated in the carbon could still be observed, indicating the excellent structural stability of $MoSe_2$/MoC/N–C nanocomposite. Compared to the 10-layered structure in Fig. 2k (or Fig. S13B2), the HRTEM image (Fig. 4j or Fig. S13B4) demonstrates that $MoSe_2$ nanodots have been exfoliated into less layers (about 4 layers) and smaller size (about 5 nm). The interlayer distance also expanded to 0.751 nm after cycling. In addition, large

 https://doi.org/10.1007/s40820-020-00511-4

areas of graphitized carbon were observed with an enlarged spacing (about 0.411 nm), slightly larger than the initial value of 0.370 nm for the pristine carbon. The expanded interlayer distance of $MoSe_2$ and carbon could be caused by the repeated insertion/extraction of Li ions [28, 36]. The smaller $MoSe_2$ nanocrystal can further provide Li storage sites, benefiting the capacity of electrode. And the increased graphitization carbon layer enhanced the electronic conductivity. These changes of electrodes material during cycling result in climbing capacities. To further examine the reinforced structure stability of $MoSe_2$/MoC/N–C, the TEM images of $MoSe_2$/MoC/N–C electrode after 500 cycles are compared in Fig. S13B5–B7. Figure S13B5 confirms that the $MoSe_2$/MoC/N–C electrode material retains integrated. As shown in Fig. S13B6 and B7, small shadow dots were still distributed in the carbon framework in $MoSe_2$/MoC/N–C electrode, implying the products were also evenly constrained in carbon framework. These results prove that $MoSe_2$/MoC/N–C connection can constrain the in situ generated $MoSe_2$ and facilitate the highly reversible conversion during cycling.

4 Conclusion

In conclusion, 3D porous $MoSe_2$/MoC/N–C nanocomposite was synthesized by a temperature-induced method. The interface bridging between $MoSe_2$ and carbon framework was tuned by $MoSe_2$/MoC/N–C connection, greatly improves the structural stability and electronic conductivity and reduces the interfacial charge resistance. Moreover, it also exhibits many features favorable for lithium-ion storage, such as $MoSe_2$ nanodots encapsulated into 3D connected carbon network to improve charge/ion transfer kinetics and minimize the effect of volume expansion; expanded interlayer spacing of $MoSe_2$ to promote lithium-ion diffusion; large electroactive surface area from N–C and rich edge defects of $MoSe_2$; and reinforced structure stability by intermediate in situ MoC. As a result, the as-prepared electrode delivered ultralong and stable cycling performance with a specific capacity of 618 mAh g^{-1} after 5000 cycles (90% capacity retention) at 2 A g^{-1}. It also shows promising potential in $LiFePO_4$//$MoSe_2$/MoC/N–C full cell (86% capacity retention at 2 A g^{-1} after 300 cycles). Inspired by the harvest of superior cell performance, in situ engineering corresponding metal carbide as interphase to connect metal dichalcogenide and carbon matrix can be developed as an innovative and effective strategy to achieve high-electrochemical-activity materials.

5 Supporting Information

Experimental section, supplementary scheme diagram of interface modification, TG, XRD, BET, SEM, EIS, CV, GITT and equations associated with this article are given in the online version or from the author.

Acknowledgements This work was supported by the National Natural Science Foundation of China (No 51872334, 51932011, 51874326, 51572299), the Natural Science Foundation of Hunan Province for Distinguished Young Scholars (2018JJ1036), and the Independent exploration and innovation Project for graduate students of central south university (2019zzts049).

Electronic supplementary material The online version of this article (https://doi.org/10.1007/s40820-020-00511-4) contains supplementary material, which is available to authorized users.

References

1. X. Xiao, H. Wang, P. Urbankowski, Y. Gogotsi, Topochemical synthesis of 2D materials. Chem. Soc. Rev. **47**, 8744–8765 (2018). https://doi.org/10.1039/c8cs00649k
2. D. Rhodes, S.H. Chae, R. Ribeiro-Palau, J. Hone, Disorder in van der waals heterostructures of 2D materials. Nat. Mater. **18**, 541–549 (2019). https://doi.org/10.1038/s41563-019-0366-8
3. A. Zavabeti, A. Jannat, L. Zhong, A.A. Haidry, Z. Yao, J.Z. Ou, Two-dimensional materials in large-areas: synthesis, properties and applications. Nano-Micro Lett. **12**, 66 (2020). https://doi.org/10.1007/s40820-020-0402-x
4. L. Lin, W. Lei, S. Zhang, Y. Liu, G.G. Wallace, J. Chen, Two-dimensional transition metal dichalcogenides in supercapacitors and secondary batteries. Energy Storage Mater. **19**, 408–423 (2019). https://doi.org/10.1016/j.ensm.2019.02.023

5. Z. Hu, Z. Wu, C. Han, J. He, Z. Ni, W. Chen, Two-dimensional transition metal dichalcogenides: interface and defect engineering. Chem. Soc. Rev. **47**, 3100–3128 (2018). https://doi.org/10.1039/c8cs00024g
6. J. Lee, C. Kim, K. Choi, J. Seo, Y. Choi et al., In-situ coalesced vacancies on $MoSe_2$ mimicking noble metal: unprecedented tafel reaction in hydrogen evolution. Nano Energy **63**, 103846 (2019). https://doi.org/10.1016/j.nanoen.2019.06.042
7. J. Xiao, Y. Zhang, H. Chen, N. Xu, S. Deng, Enhanced performance of a monolayer MoS_2/WSe_2 heterojunction as a photoelectrochemical cathode. Nano-Micro Lett. **10**, 60 (2018). https://doi.org/10.1007/s40820-018-0212-6
8. H. Xu, J. Zhu, G. Zou, W. Liu, X. Li et al., Spatially bandgap-graded $MoS_{2(1-x)}Se_{2x}$ homojunctions for self-powered visible–near-infrared phototransistors. Nano-Micro Lett. **12**, 26 (2020). https://doi.org/10.1007/s40820-019-0361-2
9. S. Chen, S. Huang, J. Hu, S. Fan, Y. Shang et al., Boosting sodium storage of $Fe_{1-x}S$/MoS_2 composite via heterointerface engineering. Nano-Micro Lett. **11**, 80 (2019). https://doi.org/10.1007/s40820-019-0311-z
10. A. Eftelthari, Molybdenum diselenide ($MoSe_2$) for energy storage, catalysis, and optoelectronics. Appl. Mater. Today **8**, 1–17 (2017). https://doi.org/10.1016/j.apmt.2017.01.006
11. X.L. Hu, W. Zhang, X.X. Liu, Y.N. Mei, Y. Huang, Nanostructured Mo-based electrode materials for electrochemical energy storage. Chem. Soc. Rev. **44**, 2376–2404 (2015). https://doi.org/10.1039/c4cs00350k
12. H. Huang, J. Cui, G. Liu, R. Bi, L. Zhang, Carbon-coated $MoSe_2$/MXene hybrid nanosheets for superior potassium storage. ACS Nano **13**, 3448–3456 (2019). https://doi.org/10.1021/acsnano.8b09548
13. F.E. Niu, J. Yang, N.N. Wang, D.P. Zhang, W.L. Fan, J. Yang, Y.T. Qian, $MoSe_2$-covered n, p-doped carbon nanosheets as a long-life and high-rate anode material for sodium-ion batteries. Adv. Funct. Mater. **27**, 1700522 (2017). https://doi.org/10.1002/adfm.201700522
14. T. Xiang, S. Tao, W.Y. Xu, Q. Fang, C.Q. Wu et al., Stable 1t-$MoSe_2$ and carbon nanotube hybridized flexible film: binder-free and high-performance li-ion anode. ACS Nano **11**, 6483–6491 (2017). https://doi.org/10.1021/acsnano.7b03329
15. J. Zheng, J. Lu, K. Amine, F. Pan, Depolarization effect to enhance the performance of lithium ions batteries. Nano Energy **33**, 497–507 (2017). https://doi.org/10.1016/j.nanoen.2017.02.011
16. Q. Yun, Q. Lu, X. Zhang, C. Tan, H. Zhang, Three-dimensional architectures constructed from transition-metal dichalcogenide nanomaterials for electrochemical energy storage and conversion. Angew. Chem. Int. Ed. **57**, 626–646 (2018). https://doi.org/10.1002/anie.201706426
17. W.C. Zhang, Y.J. Liu, Z.P. Guo, Approaching high-performance potassium-ion batteries via advanced design strategies and engineering. Sci. Adv. **5**, eaav7412 (2019). https://doi.org/10.1126/sciadv.aav7412
18. W. Zhang, J. Mao, S. Li, Z. Chen, Z. Guo, Phosphorus-based alloy materials for advanced potassium-ion battery anode. J. Am. Chem. Soc. **139**, 3316–3319 (2017). https://doi.org/10.1021/jacs.6b12185
19. K. Wang, Y. Wang, Y. Zhang, F. Liu, J. Shi et al., Bimetallic organic framework derivation of three-dimensional and heterogeneous metal selenides/carbon composite for high-performance lithium-ion batteries. Nanoscale **12**, 12623–12631 (2020). https://doi.org/10.1039/d0nr01528h
20. W.C. Zhang, W.K. Pang, V. Sencadas, Z.P. Guo, Understanding high-energy-density Sn_4P_3 anodes for potassium-ion batteries. Joule **2**, 1534–1547 (2018). https://doi.org/10.1016/j.joule.2018.04.022
21. W. Lu, Z. Yuan, Y. Zhao, H. Zhang, H. Zhang, X. Li, Porous membranes in secondary battery technologies. Chem. Soc. Rev. **46**, 2199–2236 (2017). https://doi.org/10.1039/c6cs00823b
22. K.I. Jang, K. Li, H.U. Chung, S. Xu, H.N. Jung et al., Self-assembled three dimensional network designs for soft electronics. Nat. Commun. **8**, 15894 (2017). https://doi.org/10.1038/ncomms15894
23. Z. Wu, J. Wang, R. Liu, K. Xia, C. Xuan et al., Facile preparation of carbon sphere supported molybdenum compounds (P, C and S) as hydrogen evolution electrocatalysts in acid and alkaline electrolytes. Nano Energy **32**, 511–519 (2017). https://doi.org/10.1016/j.nanoen.2017.01.014
24. S. Zhu, J.J. Li, X.Y. Deng, C.N. He, E.Z. Liu et al., Ultrathin-nanosheet-induced synthesis of 3D transition metal oxides networks for lithium ion battery anodes. Adv. Funct. Mater. **27**, 1605017 (2017). https://doi.org/10.1002/adfm.201605017
25. T. Meng, L.R. Zheng, J.W. Qin, D. Zhao, M.H. Cao, A three-dimensional hierarchically porous Mo_2C architecture: salt-template synthesis of a robust electrocatalyst and anode material towards the hydrogen evolution reaction and lithium storage. J. Mater. Chem. A **5**, 20228–20238 (2017). https://doi.org/10.1039/c7ta05946a
26. R.G. Mariano, K. McKelvey, H.S. White, M.W. Kanan, Selective increase in CO_2 electroreduction activity at grain-boundary surface terminations. Science **358**, 1187–1191 (2017). https://doi.org/10.1126/science.aao3691
27. G.Z. Fang, Q.C. Wang, J. Zhou, Y.P. Lei, Z.X. Chen et al., Metal organic framework-templated synthesis of bimetallic selenides with rich phase boundaries for sodium-ion storage and oxygen evolution reaction. ACS Nano **13**, 5635–5645 (2019). https://doi.org/10.1021/acsnano.9b00816
28. X. Zhao, W. Cai, Y. Yang, X.D. Song, Z. Neale et al., $MoSe_2$ nanosheets perpendicularly grown on graphene with Mo–C bonding for sodium-ion capacitors. Nano Energy **47**, 224–234 (2018). https://doi.org/10.1016/j.nanoen.2018.03.002
29. P. Ge, H.S. Hou, C.E. Banks, C.W. Foster, S.J. Li et al., Binding $MoSe_2$ with carbon constrained in carbonous nanosphere towards high-capacity and ultrafast Li/Na-ion storage. Energy Storage Mater. **12**, 310–323 (2018). https://doi.org/10.1016/j.ensm.2018.02.012
30. Z. Kou, T. Wang, Q. Gu, M. Xiong, L. Zheng et al., Rational design of holey 2D nonlayered transition metal carbide/nitride heterostructure nanosheets for highly efficient water oxidation. Adv. Energy Mater. **9**, 1803768 (2019). https://doi.org/10.1002/aenm.201803768

 https://doi.org/10.1007/s40820-020-00511-4

31. X. Chen, L.-P. Lv, W. Sun, Y. Hu, X. Tao, Y. Wang, Ultrasmall MoC nanoparticles embedded in 3D frameworks of nitrogen-doped porous carbon as anode materials for efficient lithium storage with pseudocapacitance. J. Mater. Chem. A **6**, 13705–13716 (2018). https://doi.org/10.1039/c8ta03176b
32. D. Vikraman, S. Hussain, K. Karuppasamy, A. Feroze, A. Kathalingam et al., Engineering the novel $MoSe_2$–Mo_2C hybrid nanoarray electrodes for energy storage and water splitting applications. Appl. Catal. B **264**, 118531 (2020). https://doi.org/10.1016/j.apcatb.2019.118531
33. J. Chen, A. Pan, Y. Wang, X. Cao, W. Zhang et al., Hierarchical mesoporous $MoSe_2$@CoSe/n-doped carbon nanocomposite for sodium ion batteries and hydrogen evolution reaction applications. Energy Storage Mater. **21**, 97–106 (2018). https://doi.org/10.1016/j.ensm.2018.10.019
34. Y. Yu, G.H. Nam, Q. He, X.J. Wu, K. Zhang et al., High phase-purity 1T′-MoS_2- and 1T′-$MoSe_2$-layered crystals. Nat. Chem. **10**, 638–643 (2018). https://doi.org/10.1038/s41557-018-0035-6
35. Q. Su, X. Cao, T. Yu, X. Kong, Y. Wang et al., Binding $MoSe_2$ with dual protection carbon for high-performance sodium storage. J. Mater. Chem. A **7**, 22871–22878 (2019). https://doi.org/10.1039/c9ta06870h
36. Y.J. Yang, D.M. Tang, C. Zhang, Y.H. Zhang, Q.F. Liang et al., "Protrusions" or "holes" in graphene: Which is the better choice for sodium ion storage? Energy Environ. Sci. **10**, 979–986 (2017). https://doi.org/10.1039/c7ee00329c
37. Z. Shi, K. Nie, Z.-J. Shao, B. Gao, H. Lin et al., Phosphorus-Mo_2C@carbon nanowires toward efficient electrochemical hydrogen evolution: composition, structural and electronic regulation. Energy Environ. Sci. **10**, 1262–1271 (2017). https://doi.org/10.1039/c7ee00388a
38. J.M. Ge, L. Fan, J. Wang, Q.F. Zhang, Z.M. Liu et al., $MoSe_2$/n-doped carbon as anodes for potassium-ion batteries. Adv. Energy Mater. **8**, 1801477 (2018). https://doi.org/10.1002/aenm.201801477
39. M. Deng, J. Qi, X. Li, Y. Xiao, L. Yang et al., MoC/C nanowires as high-rate and long cyclic life anode for lithium ion batteries. Electrochim. Acta **277**, 205–210 (2018). https://doi.org/10.1016/j.electacta.2018.04.185
40. S.P. Zhang, G. Wang, J. Jin, L.L. Zhang, Z.Y. Wen, J.H. Yang, Robust and conductive red $MoSe_2$ for stable and fast lithium storage. ACS Nano **12**, 4010–4018 (2018). https://doi.org/10.1021/acsnano.8b01703
41. Y. Liu, M. Zhu, D. Chen, Sheet-like $MoSe_2$/C composites with enhanced li-ion storage properties. J. Mater. Chem. A **3**, 11857–11862 (2015). https://doi.org/10.1039/c5ta02100f
42. M. Yousaf, Y. Wang, Y. Chen, Z. Wang, W. Aftab et al., Tunable free-standing core-shell CNT@$MoSe_2$ anode for lithium storage. ACS Appl. Mater. Interfaces **10**, 14622–14631 (2018). https://doi.org/10.1021/acsami.7b19739
43. Q. Su, X. Cao, X. Kong, Y. Wang, C. Peng et al., Carbon-encapsulated $MoSe_2$/C nanorods derived from organic-inorganic hybrid enabling superior lithium/sodium storage performances. Electrochim. Acta **292**, 339–346 (2018). https://doi.org/10.1016/j.electacta.2018.09.154
44. Z.G. Luo, J. Zhou, L.R. Wang, G.Z. Fang, A.Q. Pan, S.Q. Liang, Two-dimensional hybrid nanosheets of few layered $MoSe_2$ on reduced graphene oxide as anodes for long-cycle-life lithium-ion batteries. J. Mater. Chem. A **4**, 15302–15308 (2016). https://doi.org/10.1039/c6ta04390a
45. J.Y. Wang, C.Q. Peng, L.L. Zhang, Y.S. Fu, H. Li et al., Construction of n-doped carbon@$MoSe_2$ core/branch nanostructure via simultaneous formation of core and branch for high-performance lithium-ion batteries. Electrochim. Acta **256**, 19–27 (2017). https://doi.org/10.1016/j.electacta.2017.09.129
46. C. Zheng, C. Chen, L. Chen, M. Wei, A CMK-5-encapsulated $MoSe_2$ composite for rechargeable lithium-ion batteries with improved electrochemical performance. J. Mater. Chem. A **5**, 19632–19638 (2017). https://doi.org/10.1039/c7ta06286a
47. H. Kim, Q.H. Nguyen, I. Kim, J. Hur, Scalable synthesis of high-performance molybdenum diselenide-graphite nanocomposite anodes for lithium-ion batteries. Appl. Surf. Sci. **481**, 1196–1205 (2019). https://doi.org/10.1016/j.apsusc.2019.03.165
48. D.L. Chao, P. Liang, Z. Chen, L.Y. Bai, H. Shen et al., Pseudocapacitive Na-ion storage boosts high rate and areal capacity of self-branched 2D layered metal chalcogenide nanoarrays. ACS Nano **10**, 10211–10219 (2016). https://doi.org/10.1021/acsnano.6b05566
49. D.L. Chao, C.R. Zhu, P.H. Yang, X.H. Xia, J.L. Liu et al., Array of nanosheets render ultrafast and high-capacity Na-ion storage by tunable pseudocapacitance. Nat. Commun. **7**, 12122 (2016). https://doi.org/10.1038/ncomms12122
50. G. Zhu, T. Chen, L. Wang, L. Ma, Y. Hu et al., High energy density hybrid lithium-ion capacitor enabled by Co_3ZnC@n-doped carbon nanopolyhedra anode and microporous carbon cathode. Energy Storage Mater. **14**, 246–252 (2018). https://doi.org/10.1016/j.ensm.2018.04.009
51. A. Djire, J.B. Siegel, O. Ajenifujah, L. He, L.T. Thompson, Pseudocapacitive storage via micropores in high-surface area molybdenum nitrides. Nano Energy **51**, 122–127 (2018). https://doi.org/10.1016/j.nanoen.2018.06.045